PERGAMON

Journal of Structural Geology 23 (2001) 1741–1751

JOURNAL OF STRUCTURAL GEOLOGY

www.elsevier.com/locate/jstrugeo

Three-dimensional shape analysis of miarolitic cavities and enclaves in the Kakkonda granite by X-ray computed tomography

Tomoyuki Ohtani*, Tsukasa Nakano, Yoshito Nakashima, Hirofumi Muraoka

Geological Survey of Japan, National Institute of Advanced Industrial Science & Technology, Tsukuba, Ibaraki 305-8567, Japan

Received 12 April 2000; revised 5 February 2001; accepted 5 February 2001

Abstract

Three-dimensional shape analysis of miarolitic cavities and enclaves from the Kakkonda granite, NE Japan, was performed by X-ray computed tomography (CT) and image analysis. The three-dimensional shape of the miarolitic cavities and enclaves was reconstructed by stacked two-dimensional CT slice images with an in-plane resolution of 0.3 mm and an inter-slice spacing of 1 mm. An ellipsoid was fitted to each reconstructed object by the image processing programs. The shortest, intermediate, and longest axes of the ellipsoids fitted to miarolitic cavities had E–W, N–S, and vertical directions, respectively. The shortest axes of the ellipsoids fitted to enclaves were sub-vertical to vertical. Three-dimensional strains calculated from miarolitic cavities and enclaves have E–W and vertical shortening, respectively. The shape characteristics of miarolitic cavities probably reflect regional stress during the late magmatic stage, and those of enclaves reflect shortening by later-intruded magma or body rotation during the early magmatic stage. The miarolitic cavities may not be strained homogeneously with the surrounding granite, because the competence of minerals is different from that of the fluid-filled cavities. Although the strain markers require sufficient contrast between their CT numbers and those of the surrounding minerals, this method has several advantages over conventional methods, including the fact that it is non-destructive, expedient, and allows direct three-dimensional observation of each object.

Keywords: Miarolitic cavities and enclaves; Kakkonda granite; X-ray computed tomography

1. Introduction

Numerous techniques of strain analysis have been proposed by many structural geologists (e.g. Ramsay and Huber, 1983). Some techniques are applicable not only to two-dimensional but also three-dimensional analyses. Generally markers such as deformed fossils and xenoliths are used for analyses. Because it is difficult to measure the three-dimensional shape of individual markers directly, this aspect has been estimated statistically from the combination of several two-dimensional shapes. For example, the shapes of marker ellipses are measured on an *XZ* plane (perpendicular to foliation and parallel to lineation) and an *XY* plane (parallel to foliation), then these shapes are combined to form theoretical three-dimensional ellipsoids. Such analyses are not restricted to *XZ* and *XY* measurements, but may also use three or more arbitrary planes (Milton, 1980; Owens, 1984).

Recently, X-ray computed tomography (CT or CAT scanning) has been applied to earth sciences to visualize the internal structures of rocks. Carlson and Denison (1992) applied X-ray CT to the statistical analysis of the sizes and spatial disposition of thousands of garnet crystals in regionally metamorphosed rocks to identify mechanisms of porphyroblast crystallization. Verhelst et al. (1995) applied X-ray CT for the characterization of small scale heterogeneities of intact samples. Pyrak-Nolte et al. (1997) applied X-ray CT imaging to present quantitative aperture data for three-dimensional interconnected fracture networks embedded in intact opaque rock samples. Nakashima et al. (1997) applied microfocus X-ray CT to the three-dimensional non-destructive imaging of arrays of fluid inclusions in fluorite. Ohtani et al. (2000) used X-ray CT to clarify the heterogeneous distribution of miarolitic cavities in granite. Recent works indicate that X-ray CT is effective for visualization of three-dimensional shapes of objects in rocks. Ikeda et al. (2000) developed the image analysis technique investigating three-dimensional interconnection and the shape of the object, visualized by X-ray CT. This technique enables us to estimate the individual three-dimensional shape of objects in rocks directly and non-destructively.

* Corresponding author. Tel.: +81-298-61-3706; fax: +81-298-61-3702.
E-mail addresses: tomo-ohtani@aist.go.jp (T. Ohtani), tsukasa.nakano@aist.go.jp (T. Nakano), yoshito@gsj.go.jp (Y. Nakashima), hiro-muraoka@aist.go.jp (H. Muraoka).

0191-8141/01/$ - see front matter
PII: S0191-8141(01)00033-5

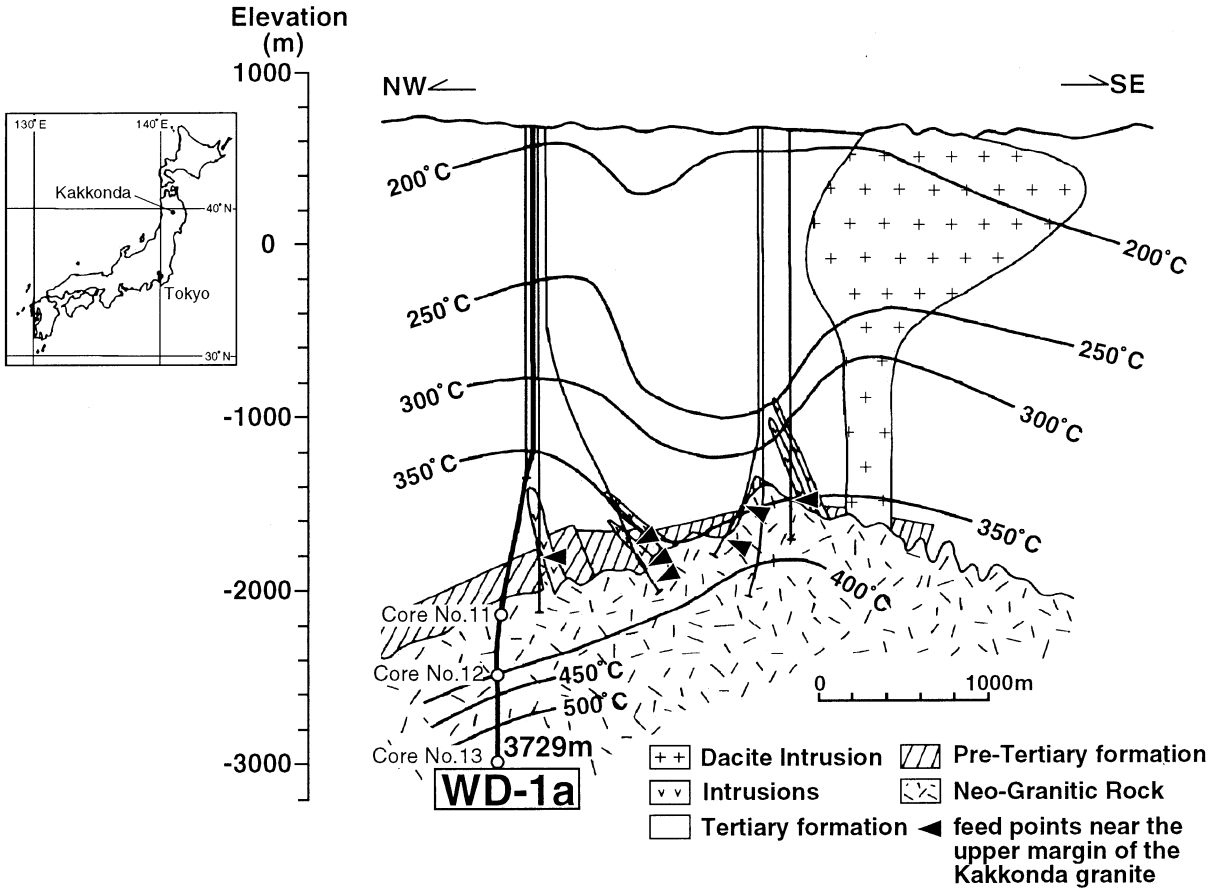

Fig. 1. Geological section of the Kakkonda geothermal field and the traces of the WD-1a and WD-1b boreholes (modified from Kato and Sato (1995) and Kato et al. (1996)).

We performed three-dimensional shape analyses of enclaves and miarolitic cavities in the Kakkonda granite, and estimated their three-dimensional strain. Three-dimensional shapes were directly reconstructed from X-ray CT images. The advantages of X-ray CT over conventional methods are that the former is: (i) capable of analyzing the individual object, (ii) non-destructive, (iii) three-dimensional, (iv) quick (typically a few hours), and (v) automatic. We describe here the method of three-dimensional shape measurement, the result of the image analyses and strain analysis, and implications for the deformation during granite emplacement at the Kakkonda geothermal field, NE Japan.

2. Regional geological setting

The Kakkonda geothermal field is located in central NE Japan, which is an active volcanic zone. This zone is mainly composed of Neogene and Quaternary volcanic rocks. The regional stress field in NE Japan has been E–W compression and vertical tension (Shimazaki et al., 1978) since 3.5 Ma (Sato, 1994).

The geology of the Kakkonda field consists mostly of Miocene and Quaternary volcanic rocks, pre-Tertiary sedimentary rocks, and Quaternary Kakkonda granite, which is presumed to be a heat source of the Kakkonda geothermal field (Doi et al., 1998). The pre-Tertiary sedimentary rocks and the Kakkonda granite are not exposed on the surface. Folds with NNW–SSE to NW–SE axes were developed in Miocene formations during the late Miocene-to-early Pliocene (Sato, 1982). Six small andesitic porphyries of unknown age trend NW–SE (Sato, 1982). Fracture analysis of hydrothermal veins revealed that the earlier minimum paleostress direction was NNE–SSW to ENE–WSW and the later one was NW–SE (Koshiya et al., 1993). The present stress state in the Kakkonda granite has been estimated from drilling-induced fractures developed from 2839 to 2963 m depth in the WD-1b borehole with a maximum horizontal stress axis of 060 to 090° (Doi et al., 1997).

3. Sample description

The samples used in this study are granite cores from the WD-1a borehole drilled at the Kakkonda geothermal field. The WD-1a borehole was drilled by the New Energy and

Industrial Technology Development Organization (NEDO) as part of the "Deep-seated Geothermal Resources Survey" project. It was 3729 m deep and the temperature at the bottom of the hole was estimated to be more than 500°C (Ikeuchi et al., 1996; Kato et al., 1996). This borehole penetrated the Quaternary and Tertiary volcanic rocks and the pre-Tertiary sedimentary rocks, and encountered the Kakkonda granite at 2860 m depth (Kato et al., 1996) (Fig. 1). The Kakkonda granite continues to the bottom of the hole. K–Ar ages of biotite and hornblende from the Kakkonda granite range from 0.068 to 0.21 Ma and 0.08 to 0.34 Ma, respectively (Kanisawa et al., 1994).

The analyzed cores were from 2936 to 2939 m (core No. 11), 3228 to 3231 m (No. 12), and 3726 to 3729 m depth (No. 13). The diameter of all three cores is 10.15 cm. No. 11 was oriented during the drilling, and No. 12 was reoriented by magnetic measurement (Kato et al., 1998). No. 11 core is medium- to fine-grained granodiorite with porphyritic texture, and Nos. 12 and 13 cores are medium-grained tonalite.

Enclaves with diameters of 5–40 mm are included in all cores from the Kakkonda granite. Miarolitic cavities with diameters of a few millimeters (abbreviated here to cavities), which result from bubbles that consist of gases and fluids emitted from magma during magma consolidation, are included from 2936.4 to 2937.6 m depth in core No. 11. Enclaves and cavities are the targets for the CT imaging in this study, as they are suitable for the X-ray CT imaging due to their size, distribution, and contrast of density and average atomic number from the host rock.

Microscopic observations revealed that a few grains of quartz in the Kakkonda granite exhibit undulatory extinction or subgrains (Fig. 2). Many fluid inclusions are included in minerals, and healed fractures are recognized in quartz grains from Nos. 11 and 12 cores based on the cathodoluminescence observation (Sasaki et al., 1998). Although mafic mineral alignment is locally recognized, this alignment shows several trends.

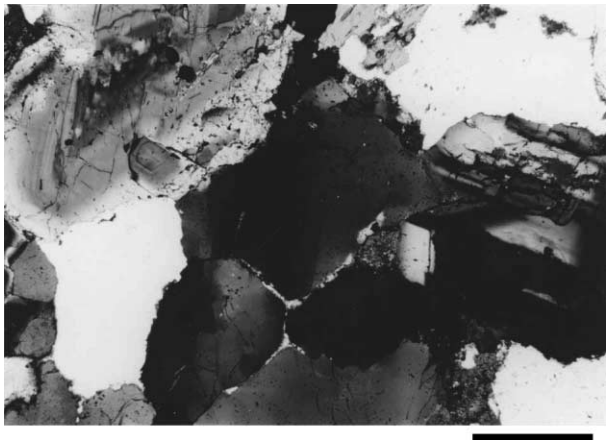

Fig. 2. Photomicrographs of the Kakkonda granite (core No. 12) from the borehole WD-1a. Undulatory extinction of quartz. Scale bar is 0.5 mm.

4. Shape measurement

X-ray CT reconstructs internal images based on the distribution of the X-ray linear absorption coefficient deduced from the projection of X-rays through a sample. The internal image is represented as an aggregate of the voxels, which are the smallest image-forming unit of an X-ray CT, and each voxel is given one value of the X-ray linear absorption coefficient. The dimensionless linear X-ray absorption coefficient is usually called CT number (χ), defined as

$$\chi = (\nu - \nu_0)/\nu_0 \times 1000 \quad (1)$$

where ν is the linear absorption coefficient of the sample and ν_0 is that of the standard reference. In medical applications, water is normally used as a standard reference for scanning human tissue. This study used the same definition of CT number as that used in medical applications. The CT number of water has a value of zero, and that of non-attenuating material, such as air, has a value of −1000. The CT number is a function of the average density and atomic number of the material in any voxel. It increases gradually in the order air, water, quartz and feldspar, biotite, hornblende, and pyrite. Thus, X-ray CT enables non-destructive imaging of minerals with different densities and average atomic numbers in the rock.

4.1. Procedure

A third-generation Hitachi Medical Corporation CT-W2000 CT scanner was used for this study. This scanner is equipped with an X-ray emission source and 768 detectors (Fig. 3). According to the manufacturer's specifications, the performance of this scanner is 0.75 mm for in-plane spatial resolution, 1 mm for minimum slice thickness, 130 kV for maximum voltage of the X-ray tube, and 160 mm for

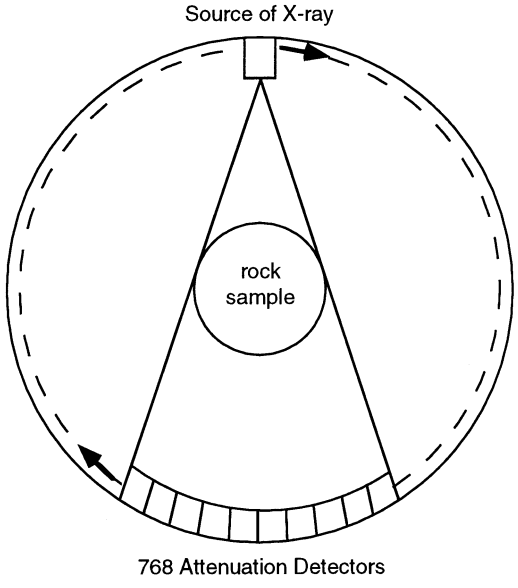

Fig. 3. The geometry of X-ray CT.

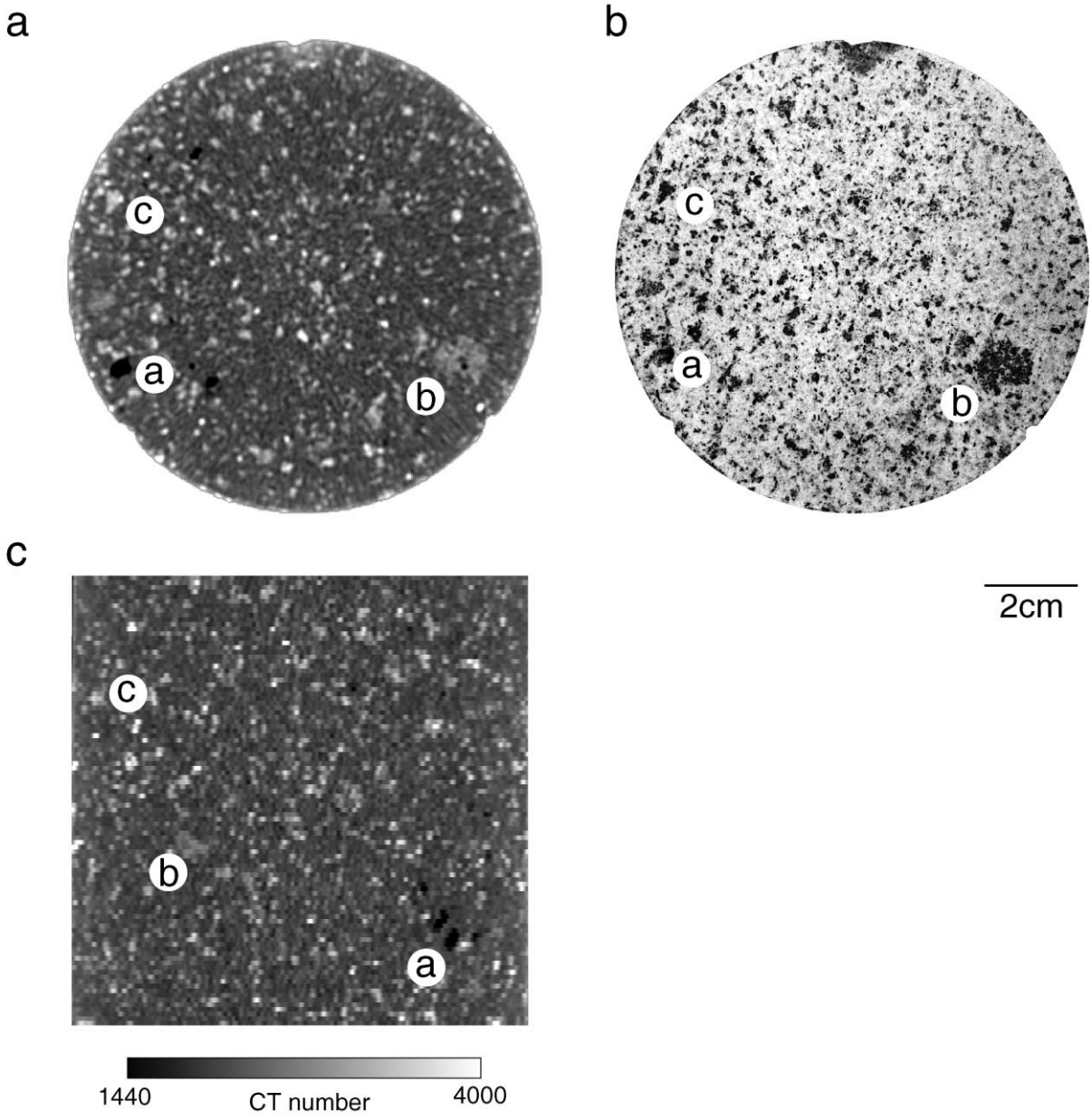

Fig. 4. (a) X-ray CT image of a granite sample from WD-1a at 2936.445 m depth. The image is perpendicular to the core axis. (b) Photograph of the polished surface. The slice positions of (a) and (b) are identical. Both images are taken from the underneath. (c) X-ray CT image parallel to the core axis from 2936.350 to 2936.446 m depth. a: Miarolitic cavity, b: enclave, c: mafic mineral.

minimum imaging diameter. The in-plane spatial resolution was confirmed by the imaging of the synthetic glass tube with an inside diameter of 0.8 mm (Ohtani et al., 2000).

The procedure of the CT imaging was as follows. First, we took contiguous two-dimensional 16-bit CT images at intervals of 1 mm. The imaging condition was 1.0 mm for slice thickness, $0.313 \times 0.313 \times 1$ mm^3 for voxel size, 4.0 s for scan time, 175 mA for X-ray tube current, 130 kV for X-ray tube voltage, 160 mm for imaging diameter, and 512×512 for matrix size. In our imaging experiments, no attempt was made to modify the original medical reconstruction algorithms. The algorithm used is one designed for the imaging of the human lungs and spinal region. Beam-hardening artifacts result from the polychromatic X-ray beam used in commercial scanners, and make quantitative analysis of CT number difficult. A copper foil (0.1 mm in thickness), a strong absorber of low-energy X-rays, was installed between the X-ray source and the sample to decrease beam hardening. The CT imaging of 99 slices took 53 min. Second, the 16-bit CT images were compared with rock textures to get binary (1-bit) images of the targets (Fig. 4). We confirmed that enclaves were represented as assemblages of voxels with a CT number more than 2350 (No. 11) and 2550 (Nos. 12 and 13), and cavities

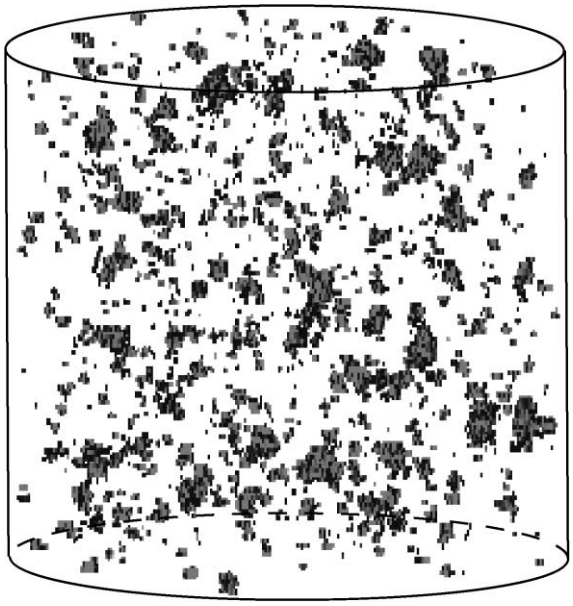

Fig. 5. Binary three-dimensional X-ray CT image of miarolitic cavities in the No. 11 core. Solid line indicates the shape of the core sample.

were less than 1500 (Ohtani et al., 2000). The threshold of core No. 11 is different from that of Nos. 12 and 13, probably due to the differences between rock type; that is, between granodiorite and tonalite.

Enclaves and cavities were reconstructed from the contiguous CT images stacked at intervals of 1 mm (Fig. 5). Ikeda et al. (2000) developed three-dimensional image analysis software including the connection analysis and the shape analysis from three-dimensional CT images. The connection analysis is known as the 'cluster labeling method' (Stauffer, 1985) in percolation theory. This analysis evaluates the connectivity of two adjacent voxels with CT numbers between given lower and upper values. When two voxels occupy the same face, the software considers them as connecting voxels. When two voxels contact only at a vertex or an edge, it considers them as separate voxels. The shape analysis consists of ellipsoids fitting to the three-dimensional object (Fig. 6) and the calculation of the directions and lengths of principal axes of ellipsoids. This fitting is performed on the assumption that the center of balance of the object corresponds to the center of the ellipsoid. First, the direction of the longest axis of the ellipsoid is determined by minimizing the second moment around the longest axis. Next, the shortest axis is determined by maximizing the second moment around the shortest axis. We define here the shortest, intermediate, and longest axes of the ellipsoid as the *a*-, *b*-, and *c*-axes, respectively. The detailed calculation process is described in Ikeda et al. (2000).

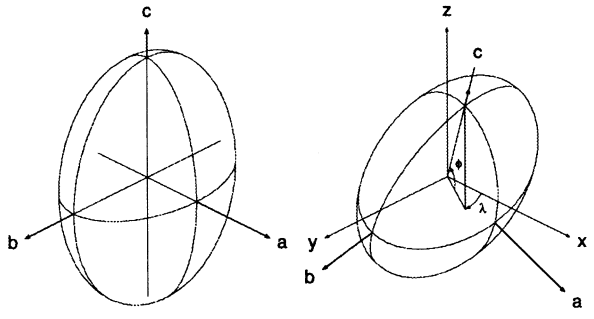

Fig. 6. Schematic images of fitted ellipsoids and their axes. Left: An ellipsoid with three arbitrary axes. The shortest, intermediate, and longest axes of the ellipsoid are defined as *a*-, *b*- and *c*-axes, respectively. Right: The direction of each axis is described by the angles between the *xyz* coordinates and the axes.

In the cavity analysis, the objects with a length parallel to the longitudinal axis of a core shorter than three voxels were excluded from the analysis, because such objects were too small to fit ellipsoids. In the enclave analysis, the voxels with a CT number higher than the given threshold indicate not only enclaves but also mafic minerals; enclaves are aggregates of mafic minerals. In order to extract only enclaves, objects smaller than 19.6 mm^2 (200 voxels) in a CT slice image were excluded from the analysis. After the connectivity analysis, we compared the extracted objects with the original CT images and selected suitable objects to fit ellipsoids and analyzed their shapes.

4.2. Results

The preferred orientation of principal axes of the ellipsoids fitted to enclaves is shown in Fig. 7. The direction of the *a*-, *b*- and *c*-axes of the ellipsoid fitted to each enclave in core No. 11 show preferences for vertical, E–W, and N–S directions, respectively. The *a*-axes in core No. 12 also concentrate around vertical. The *b*- and *c*-axes concentrate in horizontal directions. Although core No. 13 is not reoriented, the *a*-axes of ellipsoids concentrate around vertical. The graph that plots the value of *b*/*a* as abscissa and *c*/*b* as ordinate indicates that most enclaves exhibit shapes intermediate between prolate and oblate, with c/b and $b/a < 2$ (Fig. 9a). The *a*-, *b*- and *c*-axes of ellipsoids fitted to each cavity concentrate in E–W, N–S, and vertical directions, respectively (Fig. 8). Fig. 9b indicates that most cavities exhibit shapes intermediate between prolate and oblate, with c/b and $b/a < 2$. Although a few cavities seem to have prolate shapes, this probably results from the apparent connection of cavities in CT images. Adjacent cavities are rarely recognized as one object in CT images because of the finite voxel size. The average and standard deviation of the aspect ratios are summarized in Table 1.

The ellipsoids fitted to cavities are divided into four categories based on their volume to examine the influence of the voxel size and shape on the preferred axial orientation. Although the preferred orientation of the *b*-axes is not obvious in the category from 10 to 20 mm^3, that of the *a*- and *c*-axes is almost the same in all the categories (Fig. 10). This indicates that the size and shape of the voxel used in this study are adequate to analyze the shape of the cavities in the Kakkonda granite.

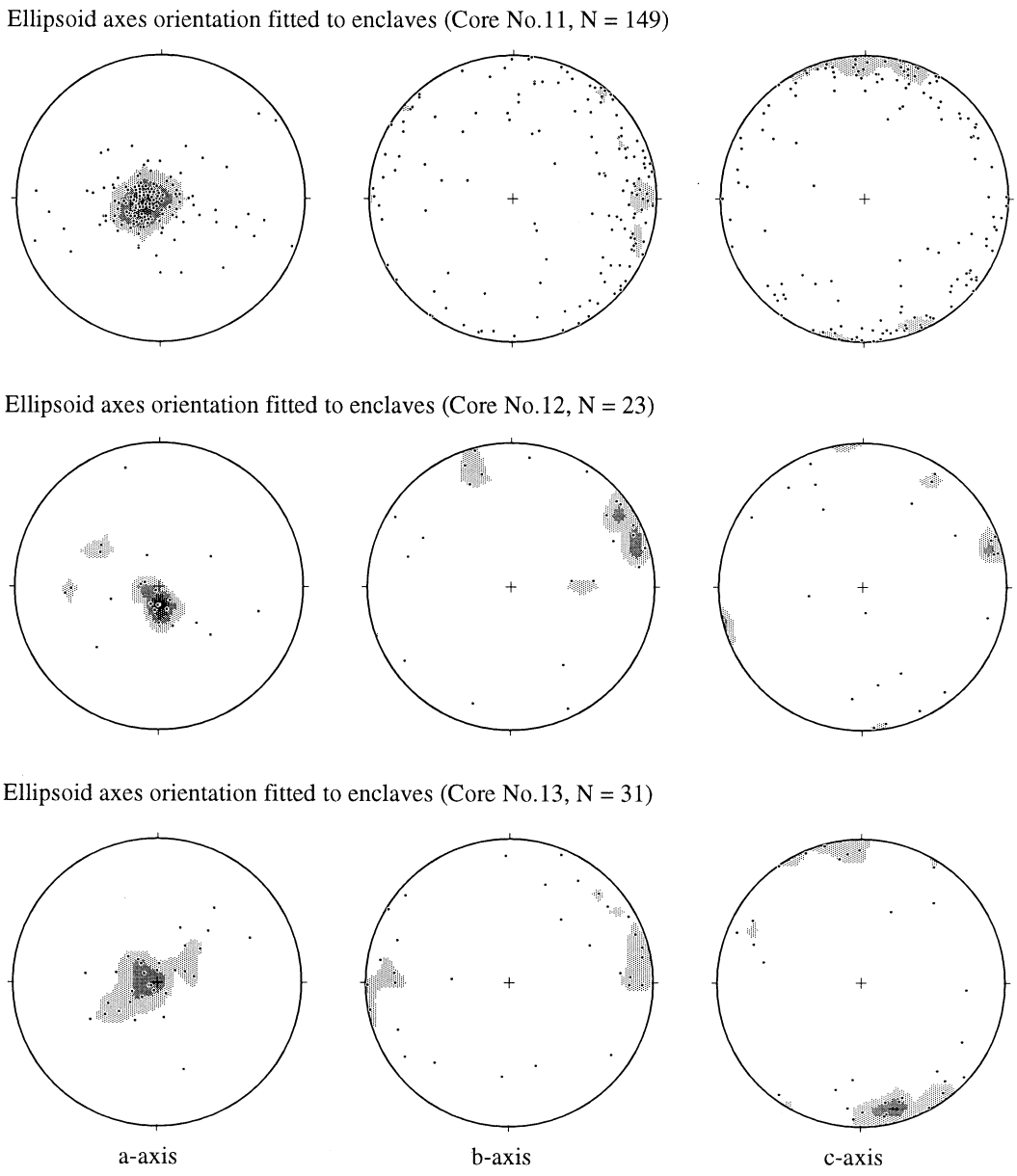

Fig. 7. Axial distribution of ellipsoids fitted to enclaves. Nos. 11 and 12 are reoriented cores. No. 13 is an unoriented core. Equal area and lower hemisphere projection. Equal area projection. Contour interval is 5.0%/1% area.

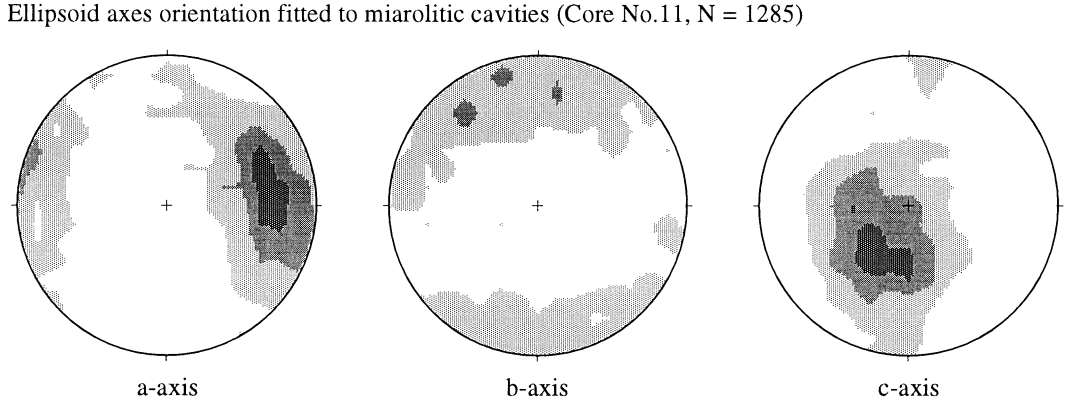

Fig. 8. Axial distribution of ellipsoids fitted to miarolitic cavities in the No. 11 core. Equal area and lower hemisphere projection. Contour interval is 1.0%/1% area.

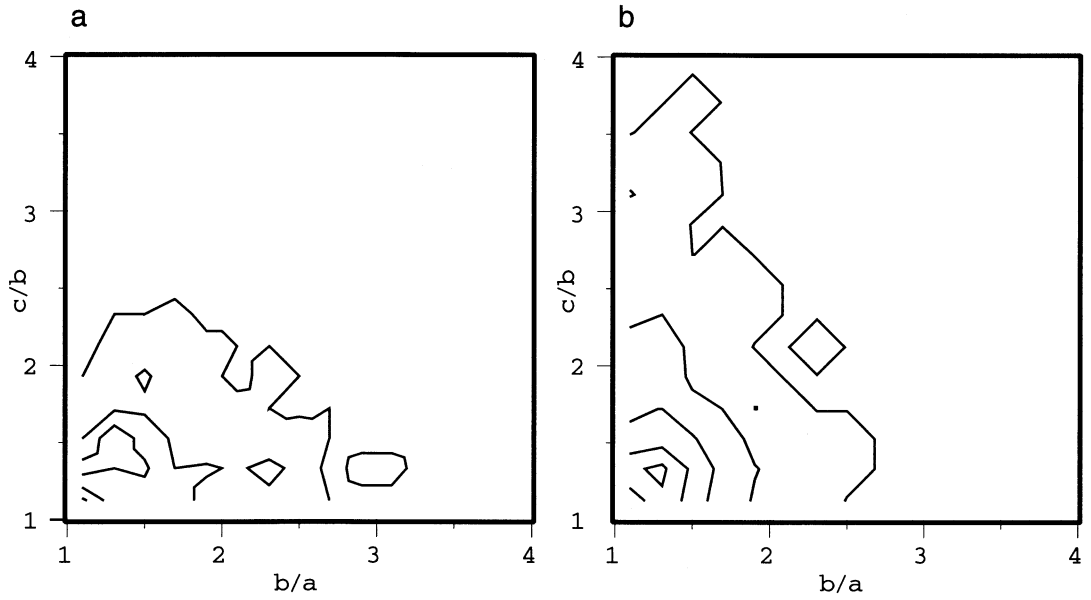

Fig. 9. Graph similar to the Flinn graph (Flinn, 1962) for representing the shape of ellipsoids fitted to enclaves and miarolitic cavities. (a) Enclaves in core Nos. 11, 12, and 13. Contour interval is 1, 5, and 10 within an area equal to 0.2 of the vertical and horizontal axes. (b) Miarolitic cavities in the No. 11 core. Contour interval is 0.1, 10, 50, 100, and 150 within the same area as (a).

5. Strain analysis

5.1. Procedure

The three-dimensional strain of the granite was estimated based on the axial ratios and directions of the reconstructed shapes of enclaves and cavities. Strain ellipsoids were calculated by the algebraic formula of Shimamoto and Ikeda (1976). This method assumes that objects are of truly ellipsoidal shape with random orientation in the undeformed state, and that they deform homogeneously with their matrix. After each ellipsoidal maker object is calculated as a 3×3 matrix, a strain ellipsoid is represented as

$$\begin{bmatrix} x & y & z \end{bmatrix} \begin{bmatrix} \bar{f} & \bar{\imath} & \bar{k} \\ \bar{\imath} & \bar{g} & \bar{\jmath} \\ \bar{k} & \bar{\jmath} & \bar{h} \end{bmatrix} \begin{bmatrix} x \\ y \\ z \end{bmatrix} = 1 \tag{2}$$

where $\bar{f}$, $\bar{g}$, $\bar{h}$, $\bar{\imath}$, $\bar{\jmath}$ and $\bar{k}$ are components of the averaged matrix. The axial ratios and directions of a strain ellipsoid are calculated from this matrix. The type and intensity of the strain are characterized by the k- and d-values of the strain ellipsoid, respectively (Flinn 1962, Ramsay and Huber 1983, pp. 199–205);

$$k = \frac{\left(R_{xy} - 1\right)}{\left(R_{yz} - 1\right)} \tag{3}$$

$$d = \sqrt{\left(R_{xy} - 1\right)^2 + \left(R_{yz} - 1\right)^2}. \tag{4}$$

5.2. Results

The results of the strain analyses are summarized in Table 2. The orientations of X-, Y- and Z-axes of cavity and enclave are approximately consistent with the trends of c-, b- and a-axes, respectively. The k-value of the cavities, close to one, indicates plane strain, and the d-value is small. The k-values of the enclaves in three cores ranging from zero to one indicate apparent flattening, and the d-values are greater than those of the cavities. The characteristics of the three-dimensional strain of the enclaves in core No. 11 are similar to those in core No. 12.

Table 1
Results of shape analyses. Parameters shown are number of measurements (n); average and standard deviation of c/b and b/a ratios of the ellipsoids fitted to the miarolitic cavities and enclaves

Core no.	Depth (m)	Object	n	Average c/b	Average b/a	Standard dev. c/b	Standard dev. b/a
No. 11	2936–2939	Miarolitic cavity	1285	1.44	1.34	0.36	0.25
No. 11	2936–2939	Enclave	149	1.49	1.82	0.34	0.67
No. 12	3228–3231	Enclave	23	1.66	1.92	0.75	0.92
No. 13	3726–3729	Enclave	31	1.52	1.63	0.40	0.42

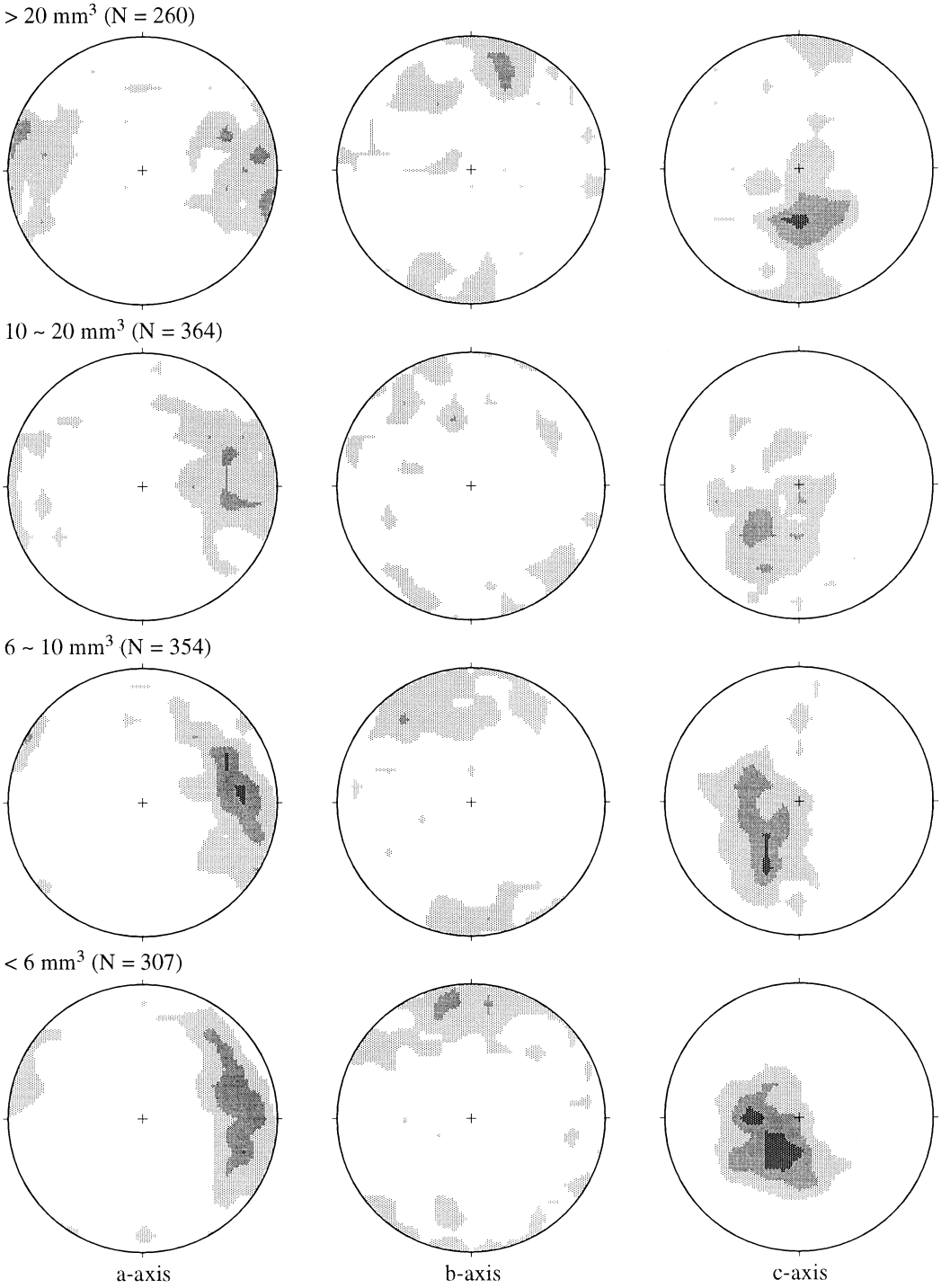

Fig. 10. Axial distribution of ellipsoids fitted to miarolitic cavities in the No. 11 core divided into four different size categories by volume. Equal area and lower hemisphere projection. Contour interval is 1.5%/1% area.

Table 2
Results of strain analyses. Parameters shown are number of measurements (*n*); *X*-, *Y*- and *Z*-axes direction of the strain ellipsoid (*X*, *Y*, *Z*); *X*/*Y* and *Y*/*Z* ratios of the strain ellipsoid; *k*- and *d*-values of the strain ellipsoid

Core no.	Depth (m)	Object	*n*	X	Y	Z	*X*/*Y*	*Y*/*Z*	*k*	*d*
No. 11	2936–2939	Miarolitic cavity	1285	220/63	350/18	086/20	1.14	1.11	1.33	0.18
No. 11	2936–2939	Enclave	149	354/02	084/10	250/81	1.14	1.79	0.17	0.80
No. 12	3228–3231	Enclave	23	009/08	099/03	209/81	1.08	1.85	0.09	0.85
No. 13	3726–3729	Enclave	31	150/04	060/04	283/84	1.26	1.48	0.55	0.54

6. Discussion

6.1. Deformation of enclaves and miarolitic cavities during magma consolidation

The characteristics of strain ellipsoids calculated from the enclaves are different from those from the cavities. This may result from different stages of shape formation. Because the enclaves are assemblages of mafic minerals, they would have existed before the cavity formation, and at higher temperature, and have been crystallized earlier than surrounding felsic minerals. In contrast, the cavities would have been generated at the later stage during magma consolidation, and at a lower temperature, because fluid and gas phases would not be released from the silicic melt under high temperature and pressure. Therefore, the shape of enclaves has probably been formed before the cavity formation. Few plastic deformational features are exhibited in minerals. This probably indicates that the cavities were deformed at the magmatic stage. Therefore, the deformation of enclaves and cavities occurred in the early and late magmatic stages, respectively.

The axial orientations of the strain ellipsoids calculated from the enclaves may be explained by shortening perpendicular to the roof of the pluton. Such shortening does not occur in a magma chamber when magma merely cools down. However, if magma continues to intrude into the magma chamber after the consolidation of its marginal part, the marginal part would be compressed by the intruding magma. If magma was intruded through multiple batches, the earlier-intruded magma would be deformed by magma intruded in later events. Ramsay (1989) demonstrated this in the case of the Chindamora batholith, Zimbabwe, in which the marginal part of the pluton was flattened by multiple magma intrusions. Another possibility is body rotation of the enclaves in the silicic melt. If, due to gravity, enclaves accumulate in horizontal layers as a function of composition or density, the shortest axis of enclaves would be vertical.

The axial orientations of the strain ellipsoid calculated from cavities could be explained by regional compression, because the axial directions of the strain ellipsoid are consistent with the regional stress state in the last 3.5 m.y. One possible reason why the *a*-axis (shortest axis) of the ellipsoids is oriented E–W is that cavities were deformed by the regional stress, and cavities were coaxially shortened in the E–W direction. Although the timing of cavity deformation is uncertain, the Kakkonda granite is so young that the regional stress field probably has not changed since the emplacement of the granite.

The cavities may be homogeneously strained with the surrounding granite. If the shapes of the cavities reflect the finite strain of the granite, the finite strain of the enclaves before cavity deformation is calculated as:

$$\mathbf{E}_1 = \mathbf{E}_2\mathbf{C}^{-1} \quad (5)$$

where $\mathbf{E}_1$ is the shape matrix of the strain ellipsoid of the enclave before the cavity deformation, $\mathbf{E}_2$ is the final shape matrix of the strain ellipsoid calculated from the enclaves, and $\mathbf{C}$ is the final shape matrix of the strain ellipsoid calculated from the cavities. The estimated aspect ratios of *X*/*Y* and *Y*/*Z* are calculated from the matrix $\mathbf{E}_1$, and these are 1.04 and 2.20, respectively. This indicates pure flattening. But because the competence of the minerals in granite is different from that of the fluid-filled cavities, the cavities may not reflect the finite strain of the granite.

These cavities show a spatially heterogeneous distribution with a steeply-dipping boundary (Ohtani et al., 2000). If strain is localized in this zone and the cavities are elongated in a vertical direction by the regional E–W compression, the steeply-dipping cavity zones could grow to the hydrothermal reservoir because vertically elongated cavities in the steeply-dipping zone easily connect. Kato and Sato (1995) reported that boreholes, with one exception, drilled in the Kakkonda granite encountered lost circulation zones near the roof of the pluton. This indicates that the hydrothermal reservoir is located along the roof of the Kakkonda granite, suggesting that a high angle structure could be dominant in the reservoir. Although no lost circulation occurred during the drilling of the WD-1a borehole in the Kakkonda granite (Muraoka et al., 1998), the presence of vertically elongated cavities implies that the cavities may be the origin of the hydrothermal reservoir along the roof of the Kakkonda granite.

Although the cavities are recognized in the Kakkonda granite, they are not common in granite; few reports have found miarolitic cavities in granite (Bearss and Janules, 1992; Candela and Blevin, 1995). The cavities in granite might be filled by hydrothermal minerals during the hydrothermal stage after the emplacement of the granite. Because the Kakkonda granite is still in the process of cooling, the cavities in the Kakkonda granite have not yet been filled.

6.2. Possibility of direct three-dimensional strain analysis

We estimated the three-dimensional shape of enclaves and cavities directly, using X-ray CT. This method is applicable to three-dimensional strain analysis. The target strain markers require enough contrast between CT numbers to create a matrix for the binary images of objects. Enclaves and cavities have different characteristic CT numbers from those of the surrounding minerals. Amygdules in volcanic rocks and conglomerates with a difference of CT number between clasts and matrix are also suitable markers for direct three-dimensional shape analysis using X-ray CT.

The size and distribution of the marker objects are also important factors in estimating their three-dimensional shapes. A suitable sample size depends on the X-ray beam energy and voxel size. Because the X-ray beam is attenuated to an object, it is harder to penetrate a larger sample. For

example, it is very difficult for the medical CT scanner used in this study to image a rock sample larger than 20 cm in diameter. The marker objects should be sufficiently larger than the voxel size to be reconstructed from the three-dimensional CT images. The X-ray beam energy and voxel size, however, depend on the device. Three-dimensional shape analysis of micron-sized objects is possible by high-resolution X-ray CT using the monochromatic X-ray beam (Coker et al., 1996) or the micro-focus X-ray tube (Nakashima et al., 1997). A scattered distribution of marker objects is desirable for the shape analysis using X-ray CT. As shown in Fig. 9b, a dense distribution of objects rarely causes an apparent connection in reconstructed images without any corrections.

7. Conclusions

Three-dimensional shape analysis of miarolitic cavities demonstrated that *a*-, *b*-, and *c*-axes of the ellipsoids fitted to miarolitic cavities concentrate in E–W, N–S, and vertical directions, respectively. The average aspect ratios of *c*/*b* and *b*/*a* are 1.44 and 1.34. Three-dimensional shape analysis of enclaves showed that the *a*-axes of the ellipsoids fitted to enclaves concentrated around vertical. The average aspect ratios of *c*/*b* and *b*/*a* are 1.49 and 1.82 in core No. 11, 1.66 and 1.92 in core No. 12, and 1.52 and 1.63 in core No. 13, respectively. The formation of the shapes of miarolitic cavities and enclaves probably occurred during the late and early magmatic stages of the Kakkonda granite, respectively.

This method of three-dimensional shape analysis is applicable to three-dimensional strain analysis. The strain ellipsoid calculated from miarolitic cavities has a *Z*-axis plunging at 20° toward 086°, a *k*-value of 1.33 and a *d*-value of 0.18. The axial orientations of the strain ellipsoid calculated from miarolitic cavities can be explained by the regional compression, which corresponds to the present stress state in northeastern Japan. Their shape, however, may not reflect rock strain of the surrounding granite. The strain ellipsoids calculated from enclaves have subvertical *Z*-axes and are oblate. The *Z*-axis orientation of the strain ellipsoids calculated from enclaves can be explained by shortening perpendicular to the roof of the pluton, or by body rotation of enclaves in the silicic melt. Although the strain markers require sufficient contrast between their CT numbers and those of the surrounding minerals, this method has several advantages over conventional methods, including the fact that it is non-destructive, expedient, and allows direct three-dimensional observation of each object.

Acknowledgements

We are grateful to S. Koshiya of Iwate University and N. Shigematsu of Waseda University for their helpful comments, and to O. Kato of Japan Metals & Chemicals Co. Ltd for core reorientation. We also thank the New Energy and Industrial Technology Development Organization (NEDO) for their permission to use core samples and publish this paper. Rigorous reviews provided by H.A. Jelsma, W.D. Carlson and T.G. Blenkinsop significantly improved this paper. Stereonets were drawn on a Macintosh computer using the public domain STEREONET v. 4.9.6 program, which was developed by R.W. Allmendinger, Cornell University. This research was supported by the New Sunshine Project (Deep-Seated Geothermal Resources Survey) of the Ministry of International Trade and Industry, Japan.

References

Bearss, G.T., Janules, B., 1992. Miarolitic cavity minerals of the Government pit, Albany New Hampshire. Rocks and Minerals 67, 158–168.

Candela, P.A., Blevin, P.L., 1995. Do some miarolitic granites preserve evidence of magmatic volatile phase permeability? Economic Geology 90, 2310–2316.

Carlson, W.D., Denison, C., 1992. Mechanisms of porphyroblast crystallization: results from high-resolution computed X-ray tomography. Science 257, 1236–1239.

Coker, D.A., Torquato, S., Dunsmuir, J.H., 1996. Morphology and physical properties of Fontainebleau sandstone via a tomographic analysis. Journal of Geophysical Research 101, 17497–17506.

Doi, N., Kato, O., Sakagawa, Y., Akaku, K., Uchida, T., 1997. Characterization of fracture and rock property of the Kakkonda Granite by FMI and other loggings. 1997 Annual Meeting, Geothermal Research Society of Japan Abstract with Programs, P8 (in Japanese).

Doi, N., Kato, O., Ikeuchi, K., Komatsu, R., Miyazaki, S., Akaku, K., Uchida, T., 1998. Genesis of the plutonic–hydrothermal system around Quaternary granite in the Kakkonda geothermal system, Japan. Geothermics 27, 663–690.

Flinn, D., 1962. On folding during three dimensional progressive deformation. Quaternary Journal of Geological Society London 118, 385–428.

Ikeda, S., Nakano, T., Nakashima, Y., 2000. Three-dimensional study on the interconnection and shape of crystals in a graphic granite by X-ray CT and image analysis. Mineralogical Magazine 64, 945–959.

Ikeuchi, K., Komatsu, R., Doi, N., Sakagawa, Y., Sasaki, M., Kamenosono, H., Uchida, T., 1996. Bottom of hydrothermal convection found by temperature measurements above 500°C and fluid inclusion study of WD-1 in Kakkonda geothermal field, Japan. Geothermal Resources Council Transactions 20, 609–616.

Kanisawa, S., Doi, N., Kato, O., Ishikawa, K., 1994. Quaternary Kakkonda granite underlying the Kakkonda geothermal field, northeast Japan. Journal of Mineralogy, Petrology and Economic Geology 89, 390–407 (in Japanese with English abstract).

Kato, O., Sato, K., 1995. Development of deep-seated geothermal reservoir bringing the Quaternary Granite into focus in the Kakkonda geothermal field, northeastern Japan. Resource Geology 45, 131–144 (in Japanese with English abstract).

Kato, O., Doi, N., Ikeuchi, K., Kondo, T., Kamenosono, H., Yagi, M., Uchida, T., 1996. Characteristics of temperature curves and fracture systems in Quaternary granite and Tertiary pyroclastic rocks of NEDO WD-1a in the Kakkonda geothermal field, Japan. Proceedings of 8th International Symposium on the Observation of the Continental Crust Through Drilling, pp. 241–246.

Kato, O., Doi, N., Sakagawa, Y., Uchida, T., 1998. Fracture systematics in and around well WD-1, Kakkonda geothermal field, Japan. Geothermics 27, 609–629.

Koshiya, S., Okami, K., Kikuchi, Y., Hirayama, T., Hayasaka, Y., Uzawa, M., Honma, K., Doi, N., 1993. Fracture system developed in the

Takinoue geothermal area. Journal of the Geothermal Research Society of Japan 15, 109–139 (in Japanese with English abstract).

Milton, N.J., 1980. Determination of the strain ellipsoid from measurements on any three sections. Tectonophysics 64, T19–T27.

Muraoka, H., Uchida, T., Sasada, M., Yagi, M., Akaku, K., Sasaki, M., Yasukawa, K., Miyazaki, S.-I., Doi, N., Saito, S., Sato, K., Tanaka, S., 1998. Deep geothermal resources survey program: igneous, metamorphic and hydrothermal processes in a well encountering 500°C at 3729 m depth, Kakkonda, Japan. Geothermics 27, 507–534.

Nakashima, Y., Hirai, H., Koishikawa, A., Ohtani, T., 1997. Three-dimensional imaging of arrays of fluid inclusions in fluorite by high-resolution X-ray CT. Neues Jahrbuch fur Mineralogie 1997 (12), 559–568.

Ohtani, T., Nakashima, Y., Muraoka, H., 2000. Three-dimensional miarolitic cavity distribution in the Kakkonda granite from borehole WD-1a using X-ray computerized tomography. Engineering Geology 56, 1–9.

Owens, W.H., 1984. The calculation of a best-fit ellipsoid from elliptical sections on arbitrarily orientated planes. Journal of Structural Geology 6, 571–578.

Pyrak-Nolte, L.J., Montemagno, C.D., Nolte, D.D., 1997. Volumetric imaging of aperture distributions in connected fracture networks. Geophysical Research Letters 24, 2343–2346.

Ramsay, J.G., Huber, M., 1983. The Techniques of Modern Structural Geology. Volume 1: Strain Analysis. Academic Press, London.

Ramsay, J.G., 1989. Emplacement kinematics of a granite diapir: the Chindamora batholith, Zimbabwe. Journal of Structural Geology 11, 191–209.

Sasaki, M., Fujimoto, K., Sawaki, T., Tsukamoto, H., Muraoka, H., Sasada, M., Ohtani, T., Yagi, M., Kurosawa, M., Doi, N., Kato, O., Kasai, K., Komatsu, R., Muramatsu, Y., 1998. Characterization of a magmatic/meteoric transition zone at the Kakkonda geothermal system, northeast Japan. Proceedings of the 9th International Symposium on Water–Rock Interaction, pp. 483–486.

Sato, K., 1982. Analysis of geological structure in the Takinoue geothermal area. Journal of the Geothermal Research Society of Japan 87, 267–275.

Sato, H., 1994. The relationship between late Cenozoic tectonic events and stress field and basin development in northeast Japan. Journal of Geophysical Research 99, 22261–22274.

Shimamoto, T., Ikeda, Y., 1976. A simple algebraic method for strain estimation from deformed ellipsoidal objects, 1. Basic theory. Tectonophysics 36, 315–337.

Shimazaki, K., Kato, T., Yamashita, K., 1978. Basic types of internal deformation of the continental plate at arc–arc junctions. Journal of Physics of the Earth 26, S66–S83.

Stauffer, D., 1985. Introduction to Percolation Theory. Taylor and Francis, Philadelphia, PA.

Verhelst, F., Vervoort, A., De Bosscher, Ph., Marchal, G., 1995. X-ray computerized tomography: determination of heterogeneities in rock samples. Proceedings of the 8th International Congress on Rock Mechanics (ISRM, Balkema Publisher) 1, pp. 105–108.